Chapter

Piezo-Optical Transducers in High Sensitive Strain Measurements

Andrey G. Paulish, Peter S. Zagubisalo, Sergey M. Churilov, Vladimir N. Barakov, Mikhail A. Pavlov and Alexander V. Poyarkov

Abstract

New piezo-optical sensors based on the piezo-optical effect for high sensitive mechanical stress measurements have been proposed and developed. The piezo-optical method provides the highest sensitivity to strains compared to sensors based on any other physical principles. Piezo-optical sensors use materials whose parameters practically not change under load or over time, therefore piezo-optical sensors are devoid of the disadvantages inherent in strain-resistive and piezoelectric sensors, such as hysteresis, parameters degradation with time, small dynamic range, low sensitivity to strains, and high sensitivity to overloads. Accurate numerical simulation and experimental investigations of the piezo-optical transducer output signal formation made it possible to optimize its design and show that the its gauge factor is two to three orders of magnitude higher than the gauge factors of sensors of other types. The cruciform shape of the transducer photoelastic element made it possible to significantly increase the stresses in its working area at a given external force. Combining compactness, reliability, resistance to overloads, linearity and high sensitivity, in terms of the all set of these parameters, piezo-optical sensors significantly surpass the currently widely used strain-resistive, piezoelectric and fiber-optic sensors and open up new, previously inaccessible, possibilities in the tasks of measuring power loads.

Keywords: piezo-optical transducers, strain gauge, sensor gauge factor, photoelasticity, optoelectronic devices

1. Introduction

Optoelectronic measurement methods are based on optical effects associated with the electromagnetic radiation interaction with matter. The polarization of the electromagnetic wave during such interaction is the most "susceptible" parameter which ensures high sensitivity of polarization-optical methods in comparison with other measurement methods [1–5]. In addition, the optical measurement method is free from electromagnetic interference and can be used in severe environmental conditions and at high temperature [6].

One of the most important directions in the development of measuring methods and sensors based on them is the monitoring of stress states in various structures both in industry and research-and-development activities. Modern and promising

strain sensors should have low weight, small size, low power, resistance to environmental influences and electromagnetic noise immunity, stability of parameters during operation, and low cost. Today, the most widely used method for strain measuring is based on the strain-resistive effect. The strain-resistive devices are used due to its relatively low cost and easy-to-use design [7]. However, such sensors have a number of unavoidable drawbacks: parameters degradation with time, hysteresis, nonlinearity, small dynamic range, low deformation sensitivity, and dramatic sensitivity to the overloads [7]. However, with the development of technologies, especially precision ones, the requirements for strain gauges increase significantly and strain-resistive gauges do not meet modern requirements.

For measuring vibrations, accelerations, acoustic signals, sensors based on the piezoelectric effect are widely used [8–12]. Such sensors performed well when measuring dynamic deformations (vibrations), but they are not suitable for measuring static loads due to the leakage of the charge induced by the load. Moreover, when such sensors are operated, both reversible and irreversible changes in their gauge factor and other characteristics are possible. This naturally limits the application conditions and is one of the most serious drawbacks of piezoelectric accelerometers.

Fiber-optic sensors are among the modern optical methods for measuring strain. A significant advantage of such sensors is the ability to implement several, up to a hundred, sensors on single optical fiber, which is used in distributed monitoring systems [13–19]. The disadvantages of such sensors include, first of all, low sensitivity (lower than that of strain-resistive gages and piezoelectric ones) and a complex system of optical measurements.

The most sensitive method for strain measuring is based on the piezo-optical effect, which consists in changing the polarization of light propagating in a transparent stressed material [7, 20]. Such sensors have a significantly higher sensitivity than strain-resistive ones due to the fundamentally high light polarization sensitivity to change in the state of the substance in which light propagates [20]. The attempts to develop the industrially usable deformation sensors based on the piezo-optical measuring transducers are known in the literature [21–24]. However, for a number of reasons, primarily of a technological nature, these developments did not lead to the appearance of piezo-optical strain gauges capable of competing with strain-resistive sensors in terms of a price/quality ratio. In the scientific literature, there are no data on the comparative analysis of the gauge factors (the main strain gauge parameter) of strain sensors based on different physical principles, which complicates the objective assessment of their advantages and disadvantages.

The purpose of this work is to develop theoretical foundations and basic design and technological solutions for creating a highly sensitive strain sensor based on a piezo-optical optoelectronic transducer. At the same time, the sensor must meet the requirements of industrial operation, significantly surpass the parameters of modern sensors based on other principles, and be devoid of drawbacks inherent in these sensors: parameters degradation with time, hysteresis, nonlinearity, small dynamic range, low sensitivity to the deformation, and high sensitivity to the overloads.

2. Comparative analysis of the sensitivity of strain gauges based on various physical principles

Here we consider the theoretical foundations of the physical effects that underlie modern strain gauges. We will also determine the gauge factor (GF) for each type of sensor so that the sensitivity of these sensors can be compared. The GF dependence on the sensor design will also be determined.

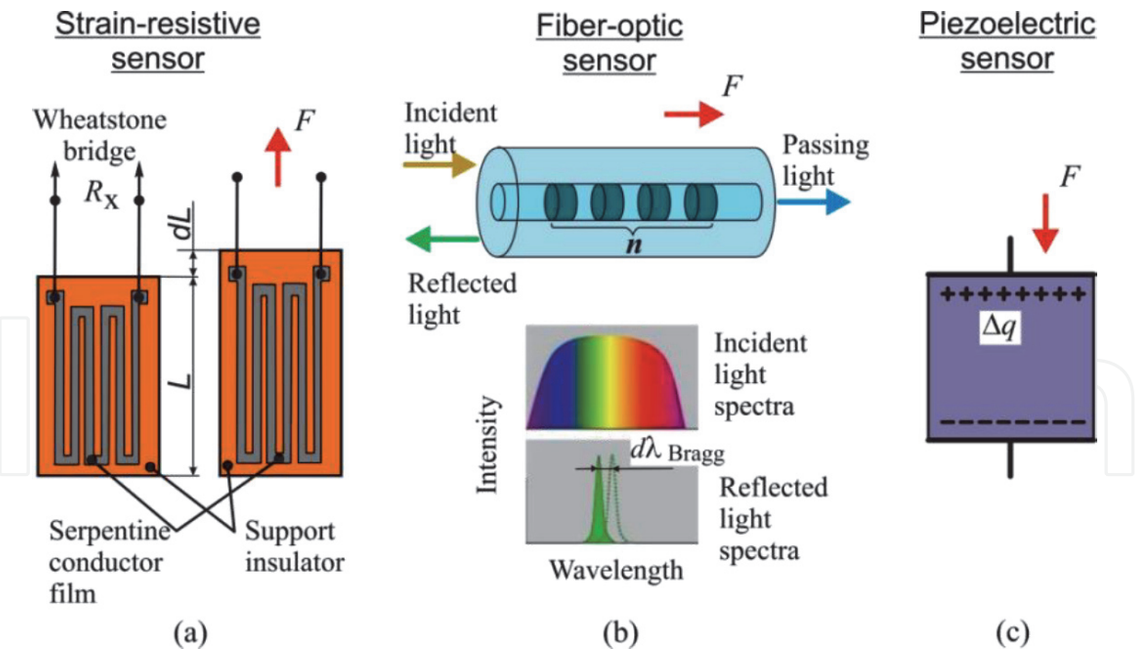

Figure 1.
Operation principle of strain gauges based on: (a) Strain-resistive, (b) Fiber–optic and (c) Piezoelectric sensors. F – Measured load, R_x – Alternating resistance, n – Effective refractive index, Δq – Stress-induced charge density.

2.1 Strain-resistive effect and strain gauge sensors

Strain-resistive gauge sensors have been well known for a long time. At first glance, the design of such a sensor looks rather simple (**Figure 1a**). A typical strain sensor design is a thin serpentine conductor film (thickness – around 0.0025 mm and length – 0.2–150 mm) deposited on a thin polymer support film. The conductor film thickness is made to be thinner and the length longer to obtain a sufficiently large resistance. Therefore, the resistance creates sufficiently large voltage for the measurements. The structure is glued to a controlled specimen and incorporated into the Wheatstone bridge [7] as an alternating resistance R_x (**Figure 1a**). The polymer film is the carrier and insulator. Their production technology is well developed and well controlled. Nevertheless, polymer films, glues, and thin metal films have low plastic deformation threshold. This leads to the problems listed above: hysteresis, nonlinearity, degradation of parameters with time, etc.

The theoretical foundations of such sensors operation, as well as the technical aspects of their use, are described in detail in work [7]. Here, the basic provisions necessary for comparing such sensors with sensors based on other physical principles are briefly presented.

It is well known that the conductor length increases $(L + dL)$, and its cross-section decreases $(S - dS)$ under the action of force F along the conductor (**Figure 1a**). In case of elastic deformation, the change in relative resistance dR/R is given by expression [7]:

$$\frac{dR}{R} = \frac{d\rho}{\rho} + \frac{dL}{L} + 2\nu\frac{dL}{L} - \nu^2\left(\frac{dL}{L}\right)^2, \tag{1}$$

where ρ is the specific resistivity and ν is the Poisson ratio, usually equal to 0.3 [7]. The strain sensitivity, gauge factor, connects the relative deformation value (dL/L) with the relative change in the measuring parameter (signal). For the strain-resistive sensor the GF is determined by the expression [7]:

$$\mathrm{GF} = \frac{dR/R}{dL/L} = \frac{d\rho/\rho}{dL/L} + 1 + 2\nu - \nu^2\left(\frac{dL}{L}\right). \quad (2)$$

It can be seen from Eq. (2) that the GF magnitude depends only on the properties of the conductor material ($d\rho/\rho$) and is *independent* of the strain gauge design. Typical gauge factor values for the materials used to create the sensors lie in the range of 2–6 [7].

2.2 Fiber-optic strain gauge sensors

The sensitive element of the fiber-optic sensors is a Bragg fiber grating which is an optical fiber with a periodically changing refractive index (**Figure 1b**). When light passes through such a structure, part of it with a specific Bragg wavelength (λ_B) is reflected, and the rest is transmitted further. The reflected light wavelength λ_B is given by the relation $\lambda_B = 2nL$, where n is the effective refractive index of the optical fiber and L is the distance between the gratings or the grating period. Stretching/compression of the fiber changes the distance L and the refractive index n resulting in a change in Bragg wavelength ($\lambda_B \pm d\lambda_B$), which is recorded by the optical system. The fiber-optic strain sensor GF is found by analogy with strain-resistive sensors [25]:

$$\mathrm{GF} = \frac{d\lambda_B/\lambda_B}{dL/L}, \quad (3)$$

where $d\lambda_B$ is the change in the reflected-light wavelength during deformation of the fiber grating and dL/L is the relative deformation of the grating. According to [25], the fiber-optic strain sensor GF is about 0.78, which is markedly lower than the strain-resistive sensor GFs. As in case of strain-resistive sensors, it does not depend on the sensor design and is determined by the properties of the fiber-optic material.

2.3 Piezoelectric effect and piezoelectric transducers

A piezoelectric transducer converts a mechanical force into an electric charge. Its operation is based on the piezoelectric effect which entails the occurrence of dielectric polarization under mechanical stresses (**Figure 1c**). The density of the electric charge induced on the piezoelectric element surface under an external load is described by the Equation [26].

$$\Delta q = d_{ij}\sigma, \quad (4)$$

where Δq is the surface charge density; d_{ij} is the piezoelectric modulus described by a 3×6 matrix with typical component values in the range of 10^{-10}–10^{-12} C/N; σ is the stress in the material under the external load. The sensitivity of these sensors is described by the piezoelectric modulus which complicates their comparison with strain-resistive and fiber-optic sensors. Similarly to Eqs. (2) and (3), the piezoelectric sensor GF should be inversely proportional to the relative deformation dL/L. Using Hooke's law $\sigma = E(dL/L)$ and Eq. (4) we get:

$$\mathrm{GF} = \frac{\Delta q}{dL/L} = \frac{d_{ij}\sigma}{dL/L} = \frac{d_{ij}E(dL/L)}{dL/L} = d_{ij}E. \quad (5)$$

It follows from Eq. (5) that the GF does not depend on the sensor design and is determined only by the piezoelectric element material properties. **Table 1** shows the values of the piezoelectric moduli and Young's moduli taken from [26, 27] and the sensitivity factors calculated by Eq. (5) for some materials widely used for the fabrication of piezoelectric sensors. It is the GF (and not the piezoelectric modulus) that is an objective sensitivity parameter of piezoelectric sensors when compared with the sensitivity of another type of sensors. For example, the piezoelectric modulus for electroactive polymers is more than two orders of magnitude greater than for other piezomaterials. However, this advantage almost vanishes due to the small elastic modulus, and, as a result, GF becomes two orders of magnitude lower than that of the other materials. **Table 1** shows that the piezoelectric sensor GFs are comparable in order of magnitude with the strain-resistive sensor GFs.

2.4 Piezo-optical effect and piezo-optical transducers

The piezo-optical effect (also called "photoelasticity") used for precision stress (deformation) measurements is known since the 1930s [28]. If a light wave with a linear (circular) polarization (**Figure 2**) is incident upon transparent material

Material	d_{ij}, 10^{-12} C/N	*E*,GPa	GF
Lead zirconate titanate (PZT)			
PZT −19	160–330	70	11,2–23,1
PZT −21	40–100	90	2,8–7,0
PZTNV-1	160–400	64	10,2–26,6
PZT-5A	274–593	60	16,4–35,6
PZT-6A	80–189	94	7,5–17,8
PZT-6B	27–71	111	3,0–7,8
Crystal quartz	2,33	78,7	0,16
Barium titanate (BaTiO3)	78	100	7,8
Solid solutions (K, Na)NbO3	80–160	104–123	8,3–19,7
Nonpolar polymers (polyethylene, rubbers, etc.)	0,1–1,0	1–3	$0,1–3{\cdot}10^{-3}$
Polar polymers (polycarbonate, polyvinyl chloride)	20–40	2,3–3,5	0,05–0,14
Electroactive polymers	30,000	$(6–1000){\cdot}10^{-6}$	< 0,03

Table 1.
Parameters of some piezoelectric materials.

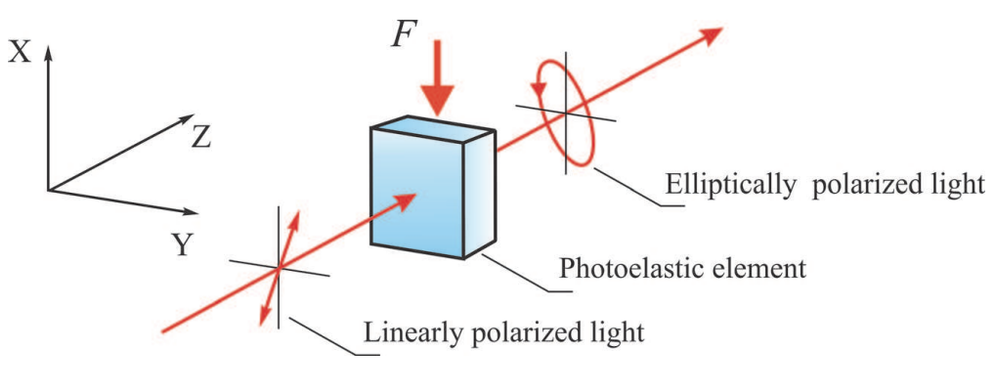

Figure 2.
Effect of photoelasticity.

(photoelastic element) under the load F, an additional phase difference Δ between the polarization components, perpendicular and parallel to the stress axis, arises due to the double refraction [20]. As a result, the light polarization in the general case becomes elliptical. The magnitude of the phase difference Δ is determined by the expression

$$\Delta = \frac{2\pi d}{\lambda}(n_{\mathrm{o}} - n_{\mathrm{e}}) = \frac{2\pi d}{\lambda}K(\sigma_y - \sigma_x) = \frac{2\pi d}{\lambda}KE\varepsilon, \tag{6}$$

here d is the path length of a light beam in the stressed material (photoelastic element thickness in the piezo-optical transducer). λ – working wavelength. n_{o} and n_{e} – refractive indexes for ordinary and extraordinary rays. K – stress-optical coefficient with typical value 10^{-11}–10^{-12} m^2/N. σ_x and σ_y – tensions along and across the applied force in a plane perpendicular to the direction of light propagation. E – Young modulus of the optical material. $\varepsilon = dL/L$ – relative deformation of the optical material. In a general case, the stresses in a photoelastic element are described by the Cauchy stress tensor σ_{ij}. Eq. (6) describes the effect of photoelasticity (**Figure 2**).

The GF for the piezo-optical transducer can be determined by analogy with the strain-resistive one, where the measuring parameter is dU/U, which is equivalent to the dR/R at constant current (Eq. (2)).

The measuring parameter for the piezo-optical effect is the phase difference Δ (Eq. (6)), which is measured by the ellipsometry techniques, so the expression for the piezo-optical GF takes the form:

$$\mathrm{GF} = \frac{\Delta}{\varepsilon} = \frac{2\pi d}{\lambda}KE. \tag{7}$$

The GF magnitude depends *not only* on the material constants (K, E) but also on the design of the piezo-optical transducer (d and λ) (see Eq. (7)). In addition, the stresses magnitude ($\sigma_y - \sigma_x$) in the photoelastic element depends strongly on the photoelastic element design to which the force is applied. This opens up the possibilities for optimizing the piezo-optical transducer parameters to increase its sensitivity to the applied force.

If fused quartz is used as the optical material, the gauge factor value $\mathrm{GF}_{\mathrm{theor}}$ can be calculated according to Eq. (7) taking into account K = 3.5 × 10^{-12} m^2/N [29], E = 70 GPa, photoelastic element thickness d = 4 mm and λ = 660 nm at 20°C (conventional LED):

$$\mathrm{GF}_{\mathrm{theor}} = \frac{2\pi \cdot 4 \cdot 10^{-3}}{0.66 \cdot 10^{-6}} 3.5 \cdot 10^{-12} \cdot 7 \cdot 10^{10} = 9330. \tag{8}$$

The GF value is more than *three orders* of magnitude higher than the strain-resistive effect values [30].

3. Piezo-optical transducer of new design

In order to achieve the set goal of the work, the following was done [30].

1. We have studied the process of piezo-optical transducer output signal generating in detail with the help of accurate numerical simulation. We determined the piezo-optical sensor GF and compared it with other types [30, 31].

2. We showed that cruciform photoelastic element (PE) allows us to significantly increase the stresses magnitude in the PE working area under the external force action and, thereby, increase the sensitivity to the force [32].

3. Fused quartz [33] was chosen as the photoelastic element material although it has a smaller stress-optical coefficient K compared to any crystals or solid polymers. However, fused quartz technology is inexpensive and well-developed. No plastic deformation exists in fused quartz and its elastic properties do not change with time. It offers a high compression damage threshold, thus, ensuring an overload resistance and a wide dynamic range of deformation measurement. Thus, there are no hysteresis and parameters degradation in such strain gauges.

4. Due to the cruciform PE, the remaining optical elements can be located within the PE dimension, and, consequently, the transducer can have its own unified casing and its technology is separated from the load cell technology. The attachment to the monitored object is carried out with the help of load elements, the design of which depends on the mounting method [34].

5. In the mounted state, the PE is under the preliminary compressive stresses along two orthogonal directions [35], which ensures: i) a reliable glueless force-closure between the PE and the load element; ii) the operation both in compression and in tension; iii) the temperature independence of the device output signal since temperature changes do not change the pre-stressed isotropy.

6. The output signal electrical circuit is located inside the transducer shielded housing and has any desired interfaces. As a result, the transducer is a complete device that does not require a secondary signal transducer as is the case with strain-resistive sensors [36].

As a result, we were able to optimize the transducer design and significantly reduce the production cost while maintaining high field-performance data. To confirm this, we compared its parameters with the parameters of most sensitive strain-resistive sensor used to calibrate the deadweight machines (see Section 6).

The optical scheme of the piezo-optical transducer is shown in **Figure 3** and consists of an optically coupled light-emitting diode (LED), a polarizer (Pol), a quarter-wave plate ($\lambda/4$), a photoelastic element (PE), two analyzers (An1, An2) and two photodetectors (PD1, PD2) [30]. The measured force F is applied to the PE.

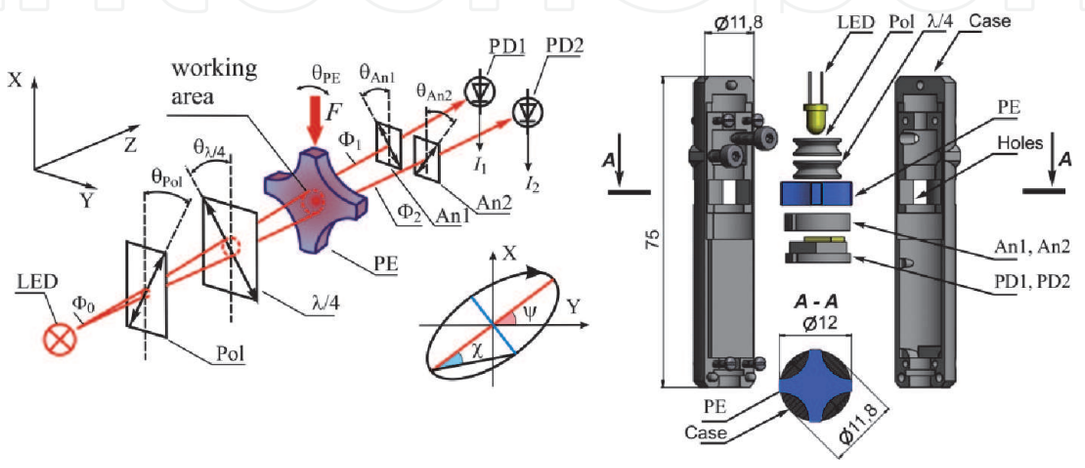

Figure 3.
Optical scheme of piezo-optical transducer (left) and its design (right).

The analyzers axes are oriented at the angle of 90°. The photoelastic element is the main component of the piezo-optical transducer. The working area of the PE is limited by the part (dashed circle in **Figure 3**) passing through which the light rays hit the photosensitive areas of the photodetectors. The rest of the PE does not participate in photodetectors signals. A feature of the transducer's optical scheme is the separation of the light beam along the front of the incident wave into two beams before falling onto the photoelastic element. This solution allows the use of film polarizers (Polaroid) reducing the optical path of light beams and, consequently, the dimensions of the converter and also allowing the use of an incoherent light source with low power consumption. The size of the optical scheme does not exceed a cubic centimeter.

The phase difference Δ between two orthogonal components of the beam polarization caused by stresses in the PE working area leads to the change in light beams intensities (Φ_1, Φ_2 in **Figure 3** on the left) incident on the photodetectors. Accordingly, it leads to the change in the output of electrical signals (I_1, I_2 in **Figure 3** on the left). The transducer electronic circuit generates a differential output signal $\sim (I_1 - I_2)/(I_1 + I_2) \sim \Delta$ which is proportional to the $\Delta\sigma = \sigma_y - \sigma_x$ (Eq. (6)) and to the applied load value.

We have optimized the PE shape and showed that the cruciform PE allows us to significantly increase the stresses magnitude in the PE working area for a given applied force [32]. The results of numerical modeling for stresses in PEs of various shapes (square, circular, rhombic, and cruciform) subjected to the same external force F = 4 N are shown in **Figure 4** [30–32]. The $\Delta\sigma = \sigma_y - \sigma_x$ isolines show the stresses distribution in PEs ($\Delta\sigma$ magnitudes are expressed in MPa). The PE working area which light passes when falling on photodetectors is shown with dashed circles. The overall dimension of all PEs was 12 × 12 mm. The calculated points are connected by straight lines just for convenience. It can be seen that the stresses are concentrated near the force application points and they are reducing considerably toward the PE center. Thus, the PE working area falls into the PE part where the stresses are minimal.

The transition to the cruciform PE and the increase in "dent" depth h (**Figure 4**) result in the stresses redistribution toward the PE center and the increase in the stress in the PE working area. For the PE shape shown in **Figure 4a** (bottom right), the increase in stresses averaged over the PE working area was 2.1 times higher compared to the square and circular shapes (dependence (1) in **Figure 4b**).

However, it is evident that the mechanical strength of a PE should go down as the "dent" h gets deeper. This issue was investigated by calculating the PE damage threshold for various PE shapes. The magnitude of stress arising in PEs of various shapes was

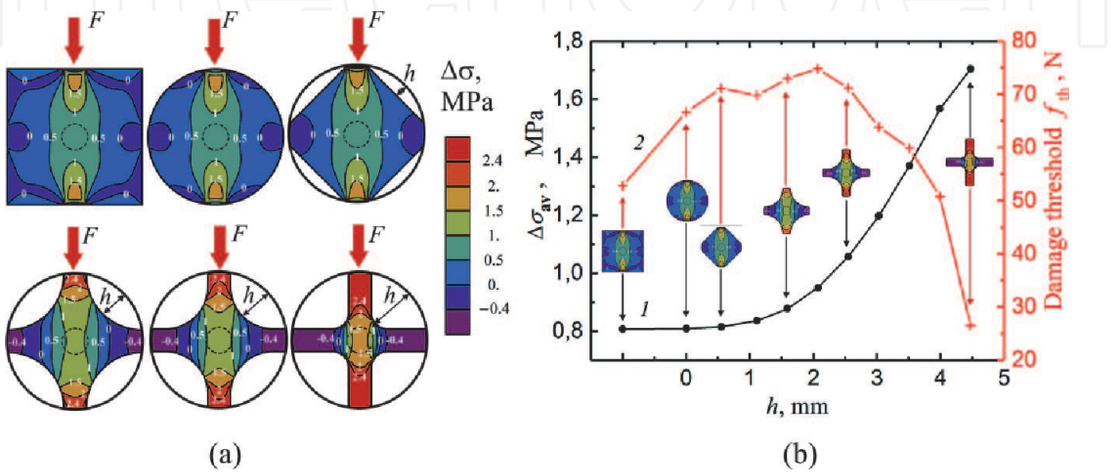

Figure 4.
(a) Isolines of stress difference Δσ for the photoelastic elements of different shapes; (b) The dependences of the stress difference $\Delta\sigma_{av}$, averaged over the PE working area (1), and damage threshold f_{th} (2) on depth h [32].

compared to the ultimate strength of quartz (51.7 MPa) [37]. The dependence (*2*) in **Figure 4b** shows the threshold force f_{th} under which the PE breakdown occurs. It can be seen that the damage threshold increases with a change in PE form from square to circular then to rhombus and even continues to grow with an increase in the "dent" depth h up to 2 mm. Further increase in h resulted in a reduction in f_{th}. The threshold begins to decrease rapidly only when $h > 3.5$ mm. Thus, at the same damage threshold for $h \approx 3.5$ mm, we have a significant increase in stresses in the PE working area.

4. Piezo-optical transducer model for numerical simulation

The mathematical models of the transducer were created for the accurate numerical simulation of its operation. The first model is for the simulation of the light parameters transformation as it passes through the optical elements of the piezo-optical transducer. The second model is for the simulation of stresses spatial distribution in the PE body and its deformation under applied force. The models, the equations used are described in detail in [30]. The initial data and the main results obtained are briefly presented here.

4.1 Simulation of the light propagation

The optical scheme of the piezo-optical transducer showed in **Figure 3** on the left was used for the simulations. The simulations were performed using the Wolfram Mathematica™ package and took into account the design of the developed transducer: the radiation diagram of LEDs used, the dimensions of the photosensitive areas of photodiodes used, light refraction in the PE, the distances between the transducer elements.

A lot of different computing methods have been developed allowing coping with cumbersome quantitative methods that have to be used to determine the output states of the electromagnetic wave amplitude and polarization. The most successful and obvious is the Muller formalism, where matrix algebra is used to describe the amplitude and polarization transformations [38–41]. The optical elements are represented in the form of a T_{ij} matrices 4×4 that describe the polarizing elements, delay elements, and rotation matrix [39]. All values in this approach are real numbers.

The connection between light intensity Φ, the degree of polarization (p), and the polarization ellipse parameters (ψ, χ) (insert in the center of **Figure 3**) with the Stokes light parameters (vector **s**) is described with the algebraic expression:

$$\mathbf{s} = \begin{bmatrix} s_0 \\ s_1 \\ s_2 \\ s_3 \end{bmatrix} = \begin{bmatrix} \Phi \\ \Phi\, p \cos 2\psi \cos 2\chi \\ \Phi\, p \sin 2\psi \cos 2\chi \\ \Phi\, p \sin 2\chi \end{bmatrix}. \tag{9}$$

In case where polarizers are arranged perpendicularly to the incident light rays and the rays are parallel to the Z-axis, the polarizer and the analyzer are described by the linear transformation according to the Muller formalism [39]:

$$\mathbf{P}(\theta) = \frac{1}{2} \begin{bmatrix} 1 & \cos 2\theta & \sin 2\theta & 0 \\ \cos 2\theta & \cos^2 2\theta & \cos 2\theta \sin 2\theta & 0 \\ \sin 2\theta & \cos 2\theta \sin 2\theta & \sin^2 2\theta & 0 \\ 0 & 0 & 0 & 0 \end{bmatrix}, \tag{10}$$

where θ is the angle of the fast axis of the polarizer measured from the X-axis to the Y-axis (**Figure 3**).

The quarter-wave plate and the photoelastic element are described by a matrix for linear delay [38]:

$$\mathbf{R}(\theta,\delta)=\begin{bmatrix}1 & 0 & 0 & 0\\ 0 & \cos^2 2\theta+\cos\delta\sin^2 2\theta & (1-\cos\delta)\cos 2\theta\sin 2\theta & -\cos\delta\sin 2\theta\\ 0 & (1-\cos\delta)\cos 2\theta\sin 2\theta & \cos\delta\cos^2 2\theta+\sin^2 2\theta & \cos 2\theta\sin\delta\\ 0 & \sin\delta\sin 2\theta & -\cos 2\theta\sin\delta & \cos\delta\end{bmatrix}. \quad (11)$$

The elements are arranged perpendicularly to the incident light rays, and the rays are parallel to the Z-axis. θ is the angle of the fast axis measured from axis X to axis Y (**Figure 3**). $\delta=\delta_y-\delta_x$ is the phase difference between the fast and the slow axes (the delay).

The Mueller matrix for refraction [41] in a PE is:

$$\mathbf{T}(\phi,\psi)=\frac{\sin 2\phi\sin 2\psi}{2\left(\sin\phi_+\cos\phi_-\right)^2}\begin{bmatrix}\cos^2\phi_-+1 & \cos^2\phi_--1 & 0 & 0\\ \cos^2\phi_--1 & \cos^2\phi_-+1 & 0 & 0\\ 0 & 0 & 2\cos\phi_- & 0\\ 0 & 0 & 0 & 2\cos\phi_-\end{bmatrix}. \quad (12)$$

where ϕ – incidence angle, ψ – refraction angle, $\phi_\pm=\phi\pm\psi$.

These matrices make it easy to study the dependence of the light intensity and polarization on the angles of all transducer elements optical axes. The results obtained make it possible to determine the tolerances for the inaccuracy of the optical elements installation. Here, for simplicity, the light rays were considered as plane wave rays that fall at right angles to the surface of each element of the optical layout. We neglected the point source of light. After substituting all Muller matrixes and taking the first components, the photocurrents I_1 and I_2 of the photodetectors PD1 and PD2 (**Figure 3**) take the form:

$$\begin{aligned}I_1&=q\frac{(4n)^2}{(n+1)^4}\Phi_0\langle\mathbf{e}_1,\mathbf{L}_1\mathbf{e}_1\rangle=4n^2q\Phi_0\frac{1+\sin\Delta_{\mathrm{PE}}}{(n+1)^4},\\ I_2&=q\frac{(4n)^2}{(n+1)^4}\Phi_0\langle\mathbf{e}_1,\mathbf{L}_2\mathbf{e}_1\rangle=4n^2q\Phi_0\frac{1-\sin\Delta_{\mathrm{PE}}}{(n+1)^4},\end{aligned} \quad (13)$$

where q – photodetector quantum efficiency, $n=n_2/n_1$ –relative refractive index, Φ_0 – light intensity, Δ_{PE} – phase shift caused by the light ray passed through the photoelastic element, $\mathbf{e}_1$ is the identity matrix, $\mathbf{L}_1$ and $\mathbf{L}_2$ are linear transformations:

$$\begin{aligned}\mathbf{L}_1&=\mathbf{P}\left(-\frac{\pi}{4}\right)\mathbf{R}(0,\Delta_{\mathrm{PE}})\mathbf{R}\left(-\frac{\pi}{4},\frac{\pi}{2}\right)\mathbf{P}(0),\\ \mathbf{L}_2&=\mathbf{P}\left(\frac{\pi}{4}\right)\mathbf{R}(0,\Delta_{\mathrm{PE}})\mathbf{R}\left(-\frac{\pi}{4},\frac{\pi}{2}\right)\mathbf{P}(0).\end{aligned} \quad (14)$$

4.2 Transducer output signal

The output signal I_{out} of the electronic circuit is

$$I_{\mathrm{out}}=k\frac{I_1-I_2}{I_1+I_2}, \quad (15)$$

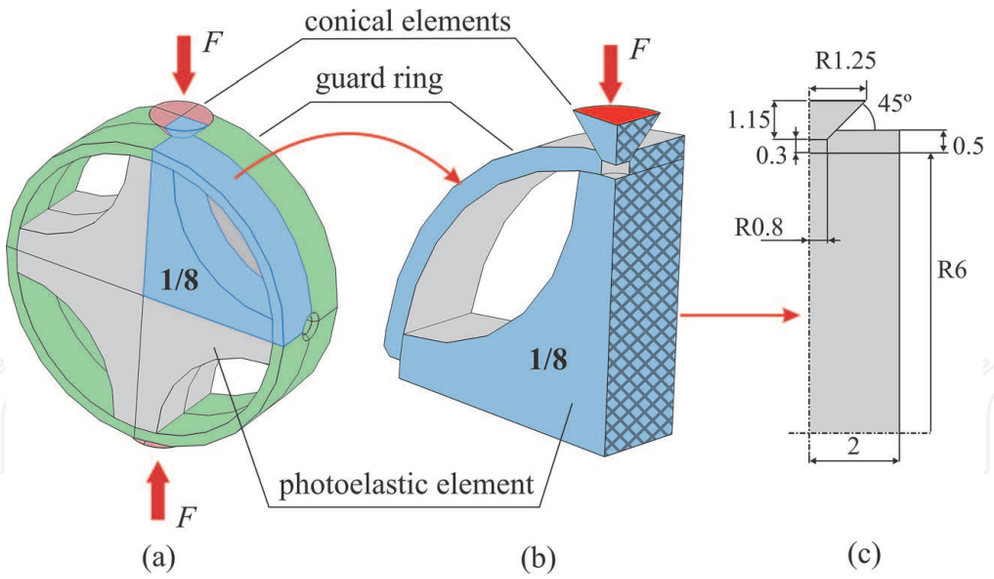

Figure 5.
(a) 3D model of the photoelastic element in the guard ring made of steel. Force F is applied to the top and bottom of the conical elements; (b) 1/8 part of the model; (c) model dimensions are indicated in millimeters [30].

where k is a proportionality factor determined by the transducer electrical circuit parameters. As a result, the signal, after the electronic circuit [36], takes the following form:

$$I_{\text{out}} = k \sin \Delta_{\text{PE}} \approx k\Delta_{\text{PE}}, \text{at } \Delta_{\text{PE}} \ll 1 \tag{16}$$

The equation shows that the change of output signal dI_{out} is directly proportional to the phase shift change $d\Delta_{\text{PE}}$ that is caused by the change of stresses in the photoelastic element.

4.3 Simulations of stresses and deformations in the photoelastic element

We used the COMSOL Multiphysics™ package and the finite-element method for the simulations of the spatial distribution of $\Delta\sigma = \sigma_y - \sigma_x$ in the PE, and PE deformation under the force F.

The 3D model of the PE encased in the steel guard ring is shown in **Figure 5a** [30, 31]. The upper and lower steel conical elements transmitted the external force to the guard ring. The embedded in COMSOL Multiphysics parameters of the material needed for the calculation of the deformation were used. Due to the PE symmetry, the simulation was only for the 1/8 part of it as shown in **Figure 5b**. The dimensions of this model part are shown in detail in **Figure 5c**.

5. Simulation and experimental results and analysis

The results of accurate numerical simulations and experiments are also detailed in [30, 31], here is a summary of them.

The strain gauge sensitivity determination was based on the experimental determination of the minimum detectable force and numerical simulation of the deformation occurring under the force action. We used the device "rhombus" with frictionless hinges to apply a calibrated force to the photoelastic element (**Figure 6a**).

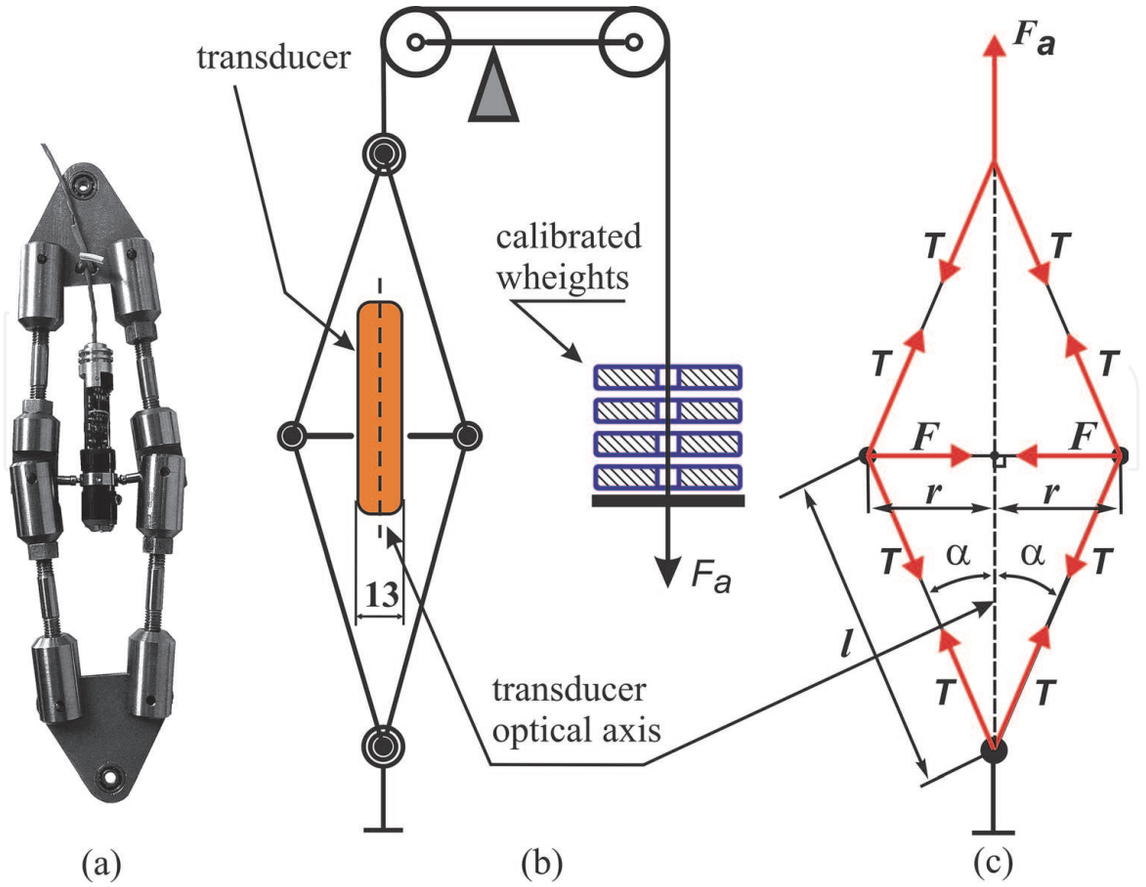

Figure 6.
(a) Rhombus photo with the transducer; (b) Force application scheme; (c) Diagram of forces in the rhombus with a fixed transducer upon the application of calibrated force F_a.

The rhombus with a fixed sensor was placed into the device for applying a calibrated force to the rhombus (**Figure 6b**). The rhombus was firmly restrained from one side and a calibrated force F_a was applied to the other side along the main axis of the rhombus symmetry pattern. The force was created by a lever mechanism with calibrated weights. The lever mechanism has the force transmission ratio of 1:8. The calibrated weight was 0.1 kgf. Thus, the weight applied to the rhombus was 0.8 kgf (7.848 N). The rhombus design ensured the force was applied to the PE in the direction perpendicular to the optical axis of the piezo-optical transducer (**Figure 6b**). To this end, the force from the rhombus was transmitting on the PE by means of conical tips that rested against the tapered holes in the guard ring (**Figure 5**). This joint provides weak stress distribution dependence in the photoelastic element on the deviation of the optical axis from the rhombus axis, due to the mobility of these elements relative to each other. In the experiments, this deviation did not exceed 1 degree, which gives the stress magnitude deviation in the PE working area (**Figure 3**) obtained by the numerical simulation is less than 0.02% and can be neglected.

A diagram of the forces generated in the rhombus with a fixed sensor upon calibrated force F_a application is shown in **Figure 6c**. T – tension force of the rhombus shoulder, l – length of the rhombus shoulder, r – radius of the photoelastic element in the guard ring, α – the angle between the shoulder and the vertical axis of the rhombus, F – the sought force applied to the photoelastic element perpendicular to the optical axis of the piezo-optical transducer.

The equations for the static forces are:

$$\begin{aligned} F_a - 2T\cos\alpha &= 0, \\ F - 2T\sin\alpha &= 0. \end{aligned} \tag{17}$$

Evaluating F we get:

$$F = F_a \mathrm{tg}\alpha = F_a \frac{r}{\sqrt{l^2 - r^2}}. \tag{18}$$

Substituting the values used: F_a = 7.848 N, r = 6.5 mm, l = 75 mm, we get the magnitude of the force applied to the photoelastic element:

$$F = 0.68 \text{ N}. \tag{19}$$

The minimum detectable force $F_{\min}$ was measured using the described experimental setup. The value obtained was used to determine the minimum detectable PE deformation $\varepsilon_{\min} = dL/L$. Further, the gauge factor was obtained by numerical simulation (GF_{sim}) and was compared with experimentally measured (GF_{exp}).
The dynamic range DR and transducer sensitivity S to force and deformation were determined as well.

5.1 Minimum detectable force

We used an analogue loop interface with current 20 mA according to standard IEC 62056–21/DIN 66258. The electric current in the analogue loop is independent of the cable resistance (its length), load resistance, EMF inductive interference, and supply voltage. Therefore, such an interface is more preferable for information transfer with remote control. The circuit allowed us to simultaneously power the transducer and generate the output signal in range 4–20 milliamps using a two-wire cable. The multimeter Agilent 34461A was used to measure the output signal and record it to a computer using the multimeter software.

Typical time dependence of the sensor output current I_{out} under the rhombus loading by the calibrated weights is shown in **Figure 7** [30, 31]. The sensor load was as follows. First, the initial preload was applied to remove the backlash. Then the rhombus was sequentially loaded with four equal calibrated weights, each providing the force of F = 0.68 N. The output signal was averaged for the four weights. The averaged output signal magnitude corresponding to force F = 0.68 N was around 300 microamperes.

The random noise ΔI_{out} of the output current I_{out} was analyzed to calculate the minimum sensor sensitivity to the applied force (noise equivalent force). We used the first 20 seconds of the time dependence, before the preload (insert in **Figure 7**) to calculate the standard output signal magnitude deviation according to the normal probability distribution for the random error (Gaussian distribution). The experimental data processing yields the standard deviation magnitude σ = 0.1278 μA, which is the commonly accepted measurement accuracy. As a result, the force measurement accuracy or the minimum detectable force is:

$$F_{\min} = 0.1278\ [\mu\text{A}] \times 0.68[\text{N}]/300[\mu\text{A}] \approx 0.00029 \text{ N} = 0.29 \text{ mN}. \tag{20}$$

Furthermore, the magnitude of the PE deformation under the force $F_{\min}$ was calculated.

5.2 Photoelastic element deformations

To simplifying the simulation, due to the symmetry of the model, the exerted force is estimated 1/4 of the experimentally applied that is 0.29 mN/4 = 0.073 mN. The accurate simulations of applied static force 0.073 mN to the model

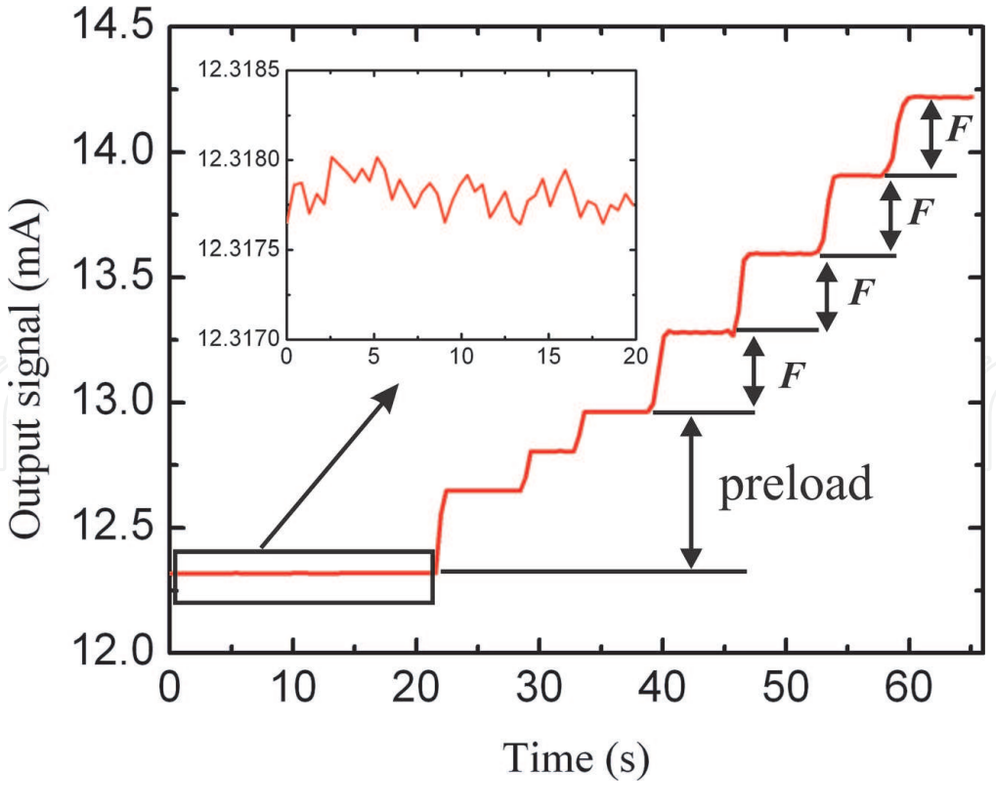

Figure 7.
Time dependence of the transducer output signal I_{out} when the load is applied consistently by means of identical calibrated weights.

(**Figure 5b**) yield the magnitude of the model deformation along the radius and along the axis of applied load $dL_{1/2} = -0.00175$ nm (i.e., this value by which the radius of the PE decreases along the applied force axis). To determine the PE diameter deformation, the result must be multiplied by 2. The resulting deformation is

$$dL = 0.0035 \text{ nm} = 3.5 \times 10^{-12} \text{ m}. \tag{21}$$

Thus, it is assumed that it is the minimum of the absolute deformation detectable by this transducer. And it corresponds to the relative deformation

$$\varepsilon_{\min} = dL/L = 3.5 \times 10^{-12} \text{ m}/12 \times 10^{-3} \text{ m} \approx 2.92 \times 10^{-10}, \tag{22}$$

where 12×10^{-3} m – the photoelastic element diameter.

This result is significantly better than that for the known industrial deformation sensors ($\varepsilon_{\min} > 10^{-8}$).

5.3 Piezo-optical transducer gauge factor

The accurate numerical simulation of the stresses which are rising in the PE working area under the applied force $F_{\min} = 0.29$ mN yields the magnitude:

$$\Delta\sigma = \sigma_y - \sigma_x = 17.11 \text{ Pa}. \tag{23}$$

The "effective" elasticity modulus E^* for present PE design can be calculated according to Hooke law:

$$E^* = \frac{\Delta\sigma}{\varepsilon} = \frac{17.11 \text{ Pa}}{2.92 \times 10^{-10}} = 58.6 \text{ GPa}. \tag{24}$$

The E^* value is somewhat smaller than the Young modulus value of fused quartz E = 70 GPa, due to the chosen PE design. Thus, Eq. (7) takes the form:

$$\mathrm{GF} = \frac{2\pi d}{\lambda} K E^*, \tag{25}$$

where the E^* value is determined by the PE design.

Now we need to define the gauge factor that works directly with photodetector output signals. If we take into account the output signal I_{out} with proportionality factor $k = 1$, we get

$$\frac{dI_{\text{out}}}{I_{\text{out}}} = \frac{I_1 - I_0}{I_0} = \frac{I_1 - I_2}{I_1 + I_2} = \mathrm{GF}_{\text{sim}} \frac{dL}{L}, \tag{26}$$

were I_0 is the I_1 signal from the photodetector PD1 without applied force ($\Delta_{\text{PE}} = 0$) and GF_{sim} is the simulated gauge factor value.

Taking into account the precise quarter-wave plate parameters (thickness $d_{\lambda/4}$ = 40 μm, $\Delta n = n_o - n_e$ =0.038 – characteristic of the quarter-wave plate birefringence), phase difference $\Delta = \Delta_{\text{PE}}$ and relative deformation magnitude $\varepsilon_{\min}$ =2.92×10^{-10}, the simulated piezo-optical transducer gauge factor GF_{sim} can be calculated:

$$\mathrm{GF}_{\text{sim}} = \frac{\sin\delta_{\lambda/4} \sin\Delta_{\text{PE}}}{\varepsilon_{\min}} = \frac{1}{\varepsilon_{\min}} \sin\left(\frac{2\pi d_{\lambda/4}}{\lambda}\Delta n\right) \sin\left(\frac{2\pi d}{\lambda} K \Delta\sigma\right) = 7389 \tag{27}$$

The simulated GF_{sim} value is somewhat smaller than the theoretical value $\mathrm{GF}_{\text{theor}}$ (Eq. (8)). This is due to the selected PE design, which determines the magnitude of the stresses $(\sigma_y - \sigma_x)$ in the PE working area for a given applied force value, and the $\sin\delta_{\lambda/4} = 0.947$ (not 1.0 for perfect quarter-wave plate).

5.4 Gauge factor dependence on photoelastic element shape

In order to determine the GF dependence on the PE shape (value of h in **Figure 4**), the relative deformation $\varepsilon = dL/L$ in Eq. (7) must be fixed in contrast to the method shown in **Figure 4**.

When varying the geometric parameters of the PE, the magnitude of the force was chosen so as to provide the same PE deformation in the direction of force application (see **Figure 4**), namely, dL = 100 nm. **Figure 8** shows the resulting dependence of GF on the parameter h [31]. It can be seen from **Figure 8** that the

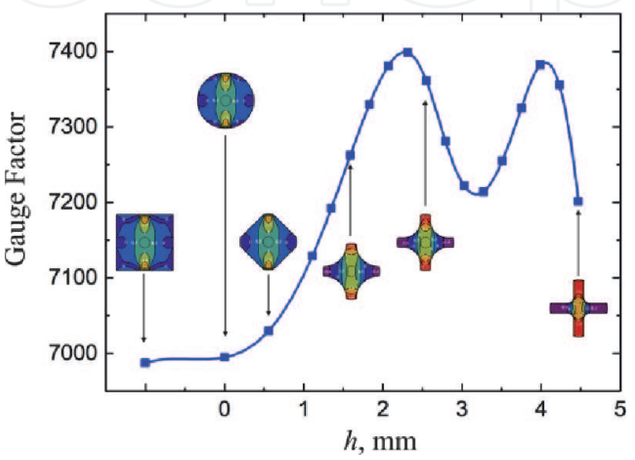

Figure 8.
Piezo-optical sensor gauge factor versus the parameter h.

dependence of GF on h is non-monotonic and contains two local maxima apparently due to the contribution of the nonlinearly changing shape of the PE side surfaces into its elastic properties. The changes in GF in the whole range of h were about 5.4% of the initial value, which is significantly less than the change in the stress difference $\Delta\sigma_{av}$ obtained in [32] and shown in **Figure 4**, which was almost 100%. This is due to the fact that as h increases, the PE stiffness (effective Young's modulus E^*) decreases in the direction of force application, which, in turn, leads to an increase in the relative deformation dL/L at the given force and a decrease in GF.

5.5 Piezo-optical transducer parameters

Experimental gauge factor. The direct measurement of the photocurrents (I_{PD1}, I_{PD2}) from the photodetectors (PD1, PD2 in **Figure 2**) yielded the experimental gauge factor GF_{exp} value

$$GF_{exp} = \frac{I_{PD1} - I_{PD2}}{I_{PD1} + I_{PD2}} = 7340. \tag{28}$$

This agrees well with the simulated gauge factor GF_{sim} and confirms the accuracy of the created transducer model.

Dynamic range. In our transducer design, as mentioned above, the PE has been affixed to the loading element in the initially stressed state that ensures the transducer operates at compressing and stretching deformation.

The transducer output signal varied from 4 to 20 mA. We set the initial output current value of 12 mA, corresponding to zero strain. The maximum change in the output signal I_{range} equal to ±8 mA, then the dynamic range DR will be

$$DR = I_{range}/\sigma = 8 \times 10^{-3}\ \text{A}/0.1278 \times 10^{-6}\ \text{A} \approx 6.2 \times 10^{4}. \tag{29}$$

The resulting dynamic range value is much higher than the known values for strain gauges.

Sensitivity. The sensitivity S (the transfer function slope) was as follows:

$$S_F = 300\ \mu\text{A}/0.68\ \text{N} \approx 441\ \mu\text{A/N to the force and} \tag{30}$$
$$S_L = 0.1278\ \mu\text{A}/0.0035\ \text{nm} \approx 36.6\ \mu\text{A/nm to the deformation.}$$

6. Testing the piezo-optical transducer

For experimental verification of the claimed parameters of the piezo-optical sensor, we carried out comparative testing with the most sensitive of the strain-resistive gauge sensor Ultra Precision LowProfile™ Load Cell Interface Force™ (**Figure 9b**) [42] used only to calibrate the deadweight machines due to its complexity and high cost. The Load Cell, selected for comparison, had the nominal load of 2000 lbs. (907.185 kg) and is based on a strain-resistive sensor. Our Load Element was a parallelepiped made of hardened steel with a transducer installed in it as shown in **Figure 9a** and had a nominal load of 1000 kg, which is close the Load Cell nominal load. Tests took place in a certified laboratory Detroit Calibration Lab Trescal [43] laboratory using a deadweight machine of the National Institute of Standards and Technology (NIST) [44].

The Load Element and then Load Cell Interface Force™ were installed in a deadweight machine where they were consistently loaded by means of calibration weights. The most striking results of comparative tests were obtained under load

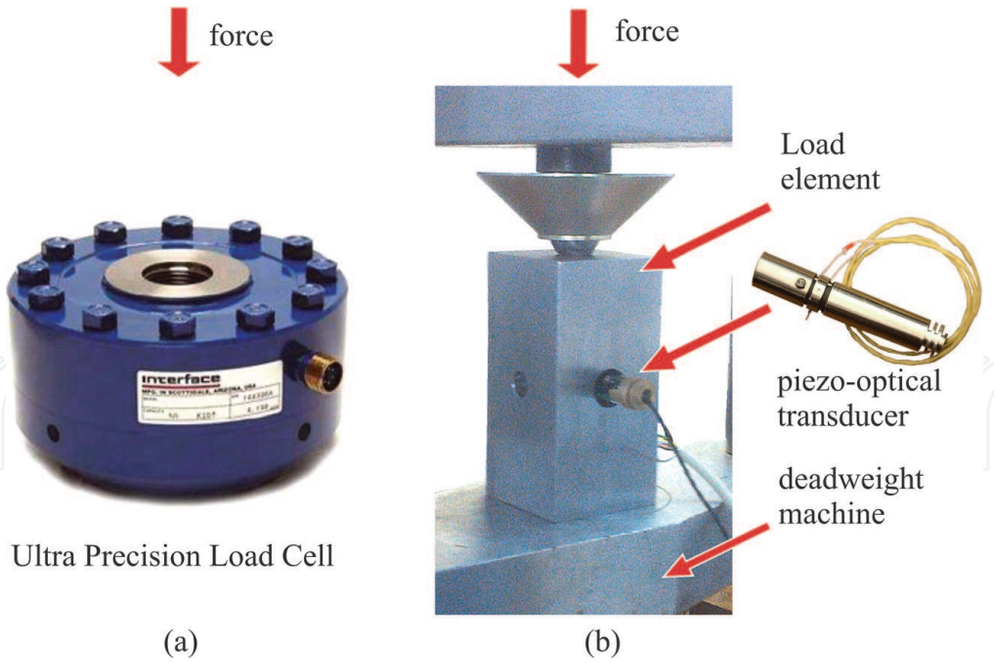

Figure 9.
(a) Ultra precision LowProfile™ Load Cell Interface force™; (b) Photos of our Load Element (left) with the piezo-optical transducer (right) and installed into a deadweight machine.

with the help of small weights, many times less than the nominal load value. The preload for both sensors was 110 lbs. and then the sensors were subsequently loaded with the calibrated weights from 1 gram to 100 grams The results are shown in **Figure 10**. The upper part of **Figure 10** corresponds to the presented piezo-optical transducer and the lower part – to the Load Cell Interface Force™. It can be seen that the piezo-optical transducer accuracy is approximately an order of magnitude higher than that for the Load Cell. This is less than the predicted calculations, and it

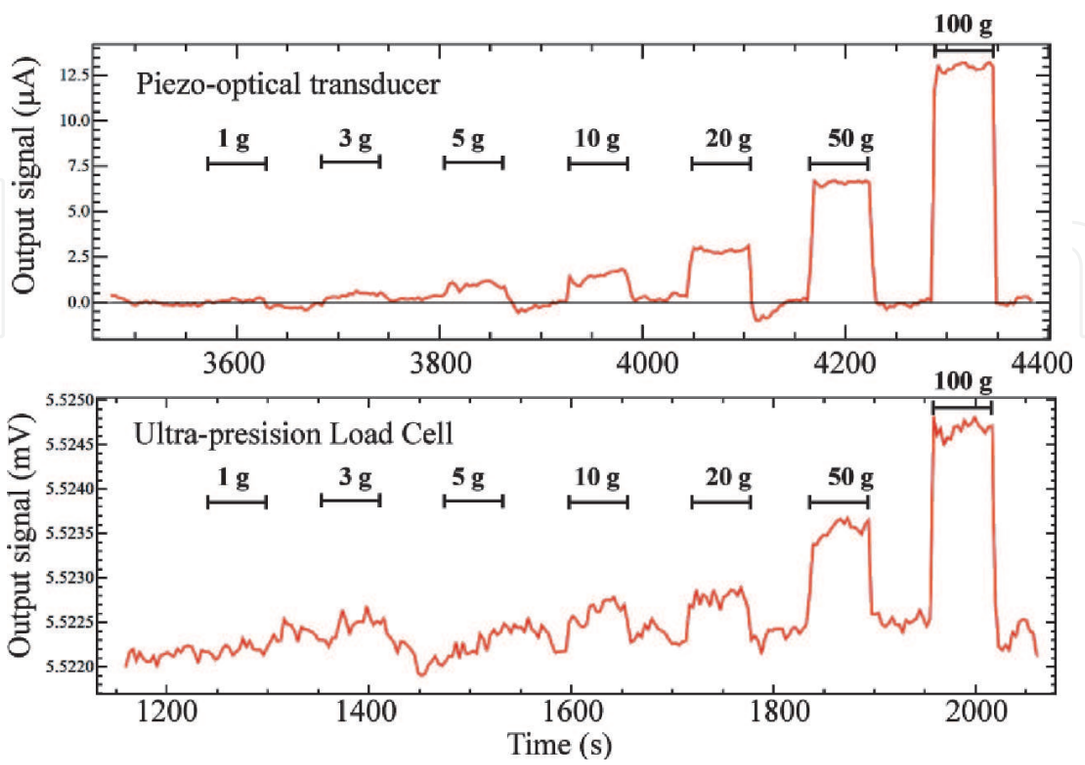

Figure 10.
Time dependence of the piezo-optical transducer (upper) and Load Cell (lower) output signals at the sequential load with calibrated weights 1, 3, 5, 10, 20, 50, 100 g.

is due to the fact that the Load Cell contains a vacuum chamber where a complex and expensive circuit is located to stabilize the output signal and reduce the noises. In our sensor, we used a design which was as simple as possible since the sensor is designed for a wide range of consumers. Nevertheless, this design showed higher sensitivity compared to the calibration Load Cell.

7. Discussion

The piezo-optical transducer operation was studied in detail theoretically, experimentally, as well as with the help of accurate numerical simulation. In order to compare the main parameters of sensors based on different physical principles, expressions for the gauge factors of strain-resistive, piezoelectric and fiber-optic sensors were proposed and analyzed. Despite the high piezoelectric modules of new piezoelectric materials (electroactive polymers), the piezoelectric sensor gauge factors are similar to strain-resistive sensor gauge factors.

It was shown that the piezo-optical sensor gauge factor, in contrast to sensors of other types, depends on the sensor design and can be improved by optimizing the PE design. The PE cruciform shape allows stresses to be concentrated in its small working volume because fused quartz used has no plastic deformation and the compressive damage threshold is very high. The piezo-optical quartz sensor gauge factor (7389), obtained by numerical simulation of stresses and deformations in the PE, is confirmed by the experimental results (7340) and is two to three orders of magnitude greater than the gauge factors of sensors based on other physical principles.

Table 2 shows that piezo-optical transducer is superior to the known industrially usable strain gauges. The high sensitivity of the piezo-optical sensor opens up new possibilities in problems of deformation measuring and stress analysis. For example, the use of only one such sensor makes it possible to control all parameters of the elevator movement: acceleration and deceleration, jerk, vibration, sound, according to International standard ISO 18738-1:2012 (E) Measurement of ride quality — Part 1: Lifts (elevators), as well as friction between the elevator car and the rails [45].

Parameter	**Sensor type**			
	Strain-resistive	**Fiber-optic**	**Piezo-electric**	**Piezo-optical**
Gauge Factor (GF)	2–4	0,78	0,1–36	> 7000
Dependence of GF on sensor design	no	no	no	yes
Deformation-to-current transfer function slope, μA/μm	—	—	80	1100–50,000
Sensitivity to the relative deformation	$\sim 10^{-6}$	$\sim 10^{-6}$	$\sim 10^{-6}$	$< 6 \times 10^{-10}$
Measurement error, %	0.05–0.1	0.25–1.0	—	0.01–0.03
Dynamic range	10^3–10^4	10^3	10^3	$> 5 \times 10^4$
Hysteresis, %	0.5	no	no	no
Overload, % of nominal	< 20	—	—	300–1000
Parameters degradation	yes	no	yes	no
Type of measured loads	Dynamic, static	Static	Dynamic	Dynamic, static

Table 2.
Comparison of some basic strain sensors parameters.

The sensor can be used in all cases where winch mechanisms are used, for example, in mines, escalators, moving walks, conveyors, cranes, etc.

Due to its high sensitivity, the sensor can be used for remote deformation monitoring by mounting at a certain distance away from the measured deformations zone: in bridge structures, cars and railway wagons weight remote control, liquids and gases flow control.

8. Conclusions

The theoretical, technological and design foundations for the highly sensitive piezo-optical transducers creation for strain gauges have been developed. It has been shown experimentally that such sensors have:

- absence of hysteresis within $\approx 1.7 \times 10^{-5}$ of the nominal load;
- high sensitivity to mechanical stresses, significantly exceeding the sensitivity of strain-resistive, piezoelectric and fiber-optic gauges and allowing to register the value of force less than 3×10^{-4} N, with a transfer function slope of ≈ 440 μA/N and ≈37 μA/nm;
- wide dynamic range, up to 6×10^{4};
- resistance to overload;
- new functionalities corresponding to the sensitivity to relative deformations less than 10^{-9}; the specified sensitivity is documented by tests in certified calibration laboratory Trescal (Detroit, USA) and other testing laboratories.

Acknowledgements

The authors are grateful to Alex Zaguskin, AZ Enterprise L.L.C. for his help in organizing the transducer test in the Detroit Calibration Lab Trescal, as well as to Robert Bolthouse for his help with the tests.

Author details

Andrey G. Paulish[1,2,3*], Peter S. Zagubisalo[1], Sergey M. Churilov[1], Vladimir N. Barakov[4], Mikhail A. Pavlov[4] and Alexander V. Poyarkov[4]

1 Novosibirsk Branch of Rzhanov Institute of Semiconductor Physics, SBRAS, Technological Design Institute of Applied Microelectronics, Novosibirsk, Russian Federation

2 Novosibirsk State Technical University, Novosibirsk, Russian Federation

3 National Research Tomsk State University, Tomsk, Russian Federation

4 Firma PODIY, Ltd., Moscow, Russian Federation

*Address all correspondence to: paulish63@ngs.ru

References

[1] Vinter B, Rosencher E, Piva P. G. Optoelectronics. Cambridge University Press CUP; 2002. 744 p. ISBN: 10: 0521778131/ISBN: 13: 9780521778138.

[2] Parker M A. Physics of Optoelectronics. Boca Raton. CRC Press Taylor & Francis Group; 2005. 766 p. ISBN:13: 9780824-53856

[3] Paulish A, Fedorinin V, Levina A. Optoelectronics in Measurement of Physical Magnitudes. New York: Nova Science Publishers, Inc.; 2011. 63 p. ISBN: 9781617610943

[4] Kasap S. O. Optoelectronics & photonics: principles & practices. 2nd English ed. Boston: Pearson Education Limited; 2013. 544 p. ISBN:13: 9780132151498.

[5] Dutta N. K, Zhang X. Optoelectronic Devices. Singapore: World Scientific Publishing Company; 2018. 588 p. ISBN: 13: 9789813236691.

[6] Doyle J. Modern experimental stress analysis. Chichester: J.Wiley& Sons; 2004. p. 158–170. DOI: 10.1002/ 0470861584.ch3.

[7] Kobayashi A. Handbook on Experimental Mechanics. Englewood Cliffs, NJ: Prentice-Hall, Inc; 1987. 1002 p. ISBN:13: 9780133777062

[8] Qiu L, Deng X, Yuan S, Huang Y, Ren Y. Impact monitoring for aircraft smart composite skins based on a lightweight sensor network and characteristic digital sequences. IEEE Sensors Journal. 2018;**18**:2218-2244. DOI: 10.3390/s18072218

[9] de Inestrillas Á, Camarena F, Cabo M, Barreiro J, Reig A. Design and performance of a metal-shielded piezoelectric sensor. IEEE Sensors Journal. 2017;**17**:1284. DOI: 10.3390/ s17061284

[10] Vitola J, Pozo F, Tibaduiza D and Anaya M. distributed piezoelectric sensor system for damage identification in structures subjected to temperature changes. IEEE Sensors Journal 2017;**17**: 1252. DOI: 10.3390/s17061252.

[11] Li M, Cheng W, Chen J, Xie R, Li X. A high performance piezoelectric sensor for dynamic force monitoring of landslide. IEEE Sensors Journal. 2017;**17**: 394. DOI: 10.3390/s17020394

[12] Rade D, de Albuquerque E, Figueira L, Carvalho J. Piezoelectric driving of vibration conveyors: An experimental assessment. IEEE Sensors Journal. 2013;**13**: 9174-9182. DOI: 10.3390/s130709174

[13] Wei P, Han X, Xia D, Liu T, Lang H. Novel fiber-optic ring acoustic emission sensor. Sensors. 2018;**1**:215. DOI: 10.3390/s18010215

[14] Liang H, Jia P, Liu J, Fang G, Li Z, Hong Y, et al. Diaphragm-free fiber-optic Fabry-Perot interferometric gas pressure sensor for high temperature application. IEEE Sensors Journal. 2018; **18**:1011. DOI: 10.3390/s18041011

[15] Sbarufatti C, Beligni A, Gilioli A, Ferrario M, Mattarei M, Martinelli M, et al. Strain wave acquisition by a fiber optic coherent sensor for impact monitoring. Materials. 2017;**10**:794-809. DOI: 10.3390/ma10070794

[16] Yang N, Su J, Fan Z, Qiu Q. High precision temperature insensitive strain sensor based on fiber-optic delay. IEEE Sensors Journal. 2017;**17**:1005. DOI: 10.3390/s17051005

[17] Peled Y, Motil A, Kressel I, Tur M. Monitoring the propagation of mechanical waves using an optic fiber distributed and dynamic strain sensor based on BOTDA. Optics Express. 2013; **21**:10697-10705. DOI: 10.1364/ OE.21.010697

[18] Wild G, Hinckley S. Acousto-ultrasonic optical fiber sensors: Overview and state-of-the-art. IEEE Sensors Journal. 2008;**8**:1184-1193. DOI: 10.1109/JSEN.2008.926894

[19] Drissi-Habti M, Raman V, Khadour A, Timorian S. Fiber optic sensor embedment study for multi-parameter strain sensing. IEEE Sensors Journal. 2017;**17**:667. DOI: 10.3390/s17040667

[20] Frocht M. Photoelasticity. New York: Wiley-Interscience; 1948. Vol. 1. p. 432

[21] Piezooptical measuring transducer, by Slezinger I, Belitsky G, Shiryaev V, Mironov J. Patent US 4010632. 1977, Mar. 08. [Internet] Available: https://patents.google.com/patent/US4010632A/ja [Accessed: 2020-06-01].

[22] Photoelastic measuring transducer and accelerometer based thereon, by Trainer M. Patent US 4648274. 1987, Mar. 10. [Internet]. Available: https://patents.google.com/patent/US4010632A/ja [Accessed: 2020-06-01].

[23] Photoelastic neural torque sensor, by Discenzo F. Patent US 5723794. 1998, Mar. 03. [Internet]. Available:https://www.google.com/patents/US5723794 [Accessed: 2020-06-01].

[24] System and method for sensing torque on a rotating shaft, by Discenzo F. Patent US 6948381. 2005, Sep. 27. [Internet] Available: http://www.google.ch/patents/US6948381 [Accessed: 2020-06-01].

[25] Klerex T, Gunter B. Deformation measurement: Fiber optic sensors from HBM. ELECTRONICS: Science, Technology, Business. 2008;**1**:76-78

[26] Gautschi G. Piezoelectric Sensorics: Force Strain Pressure Acceleration and Acoustic Emission Sensors Materials and Amplifiers. Berlin: Springer-Verlag; 2002. 264 p. ISBN: 13:9783662047323

[27] Lushcheikin G. New polymer-containing piezoelectric materials. Fizika Tverdogo Tela. 2006;**48**:963-964

[28] Coker G, Filon L. A Treatise on Photo-Elasticity. Cambridge: University Press; 1931. 624 p

[29] Richard P. Birefringence dispersion in fused silica for DUV lithography. Proceedings SPIE.Optical Microlithography XIV. 2001;**4346**. DOI: 10.1117/12.435666

[30] Paulish A, Zagubisalo P, Barakov V, Pavlov M, PoyarkovA. Piezo-optical transducer for high sensitive strain gauges. IEEE Sensors Journal 2018; **18**: 8318–8328. DOI: 10.1109/JSEN.2018.2865917.

[31] Paulish A, Zagubisalo P, Barakov V, Pavlov M. Experimental investigation of a Piezo-optical transducer for highly sensitive strain gauges. Optoelectronics, Instrumentation and Data Processing. 2018;**54**:175-180. DOI: 10.3103/S8756699018020097

[32] Paulish A, Zagubisalo P. A Photoelastic element for Piezooptic strain gauges. Technical Physics Letters. 2015;**41**:632-634. DOI: 10.1134/S1063785015070135

[33] Musgraves JD, Hu J, Calvez L, editors. Springer Handbook of Glass. Cham: Springer Nature Switzerland AG; 2019. 1841 p. ISBN: 9783319937267

[34] Strain transducer, by Paulish A, Barakov V, Poyarkov A. Patent RU 2564691.2014, Feb. 04. [Internet] Available from: https://new.fips.ru/archive/pat/2015full/2015.10.10/doc/runwc2/000/000/002/564/691/document.pdfhttps://new.fips.ru/archive/pat/2015full/2015.10.10/doc/runwc2/000/000/002/564/691/document.pdf [Accessed: 2020-06-01].

[35] Tensometric transducer, by Paulish A, Poyarkov A, Shatov V,

Rafailovich A, Fedorinin V. Patent US 8,887,577. 2010, Apr.23. [Internet] Available from: https://patentimages.storage.googleapis.com/bd/b9/d8/0c7298424d783d/US8887577.pdf [Accessed: 2020-06-01].

[36] Piezooptic converter signal processing device, by Paulish A, Pavlov M, Barakov V, Poyarkov A. Patent RU 2565856.2014, July 08. [Internet] Available: https://new.fips.ru/archive/pat/2015full/2015.10.20/doc/runwc1/000/000/002/565/856/document.pdf [Accessed: 2020-06-01].

[37] Driggers R G. Encyclopedia of Optical Engineering. Vol. 1. New York: Marcel Dekker Inc; 2003. p. 205

[38] Udd E. Fiber Optic Sensors: An Introduction for Engineers and Scientists. 2nd ed. Inc.: John Wiley & Sons; 2011. 512 p. ISBN: 9780470126844

[39] Theocaris P, Gdoutos E. Matrix Theory of Photoelasticity. New-York: Springer-Verlag; 1979. 352 p. ISBN: 0387088997

[40] Nye J. Physical Properties of Crystals, their Representation by Tensor and Matrix. Oxford: Clarendon Press; 1985. 329 p. ISBN: 019851165 5 (pbk.)

[41] Goldstein D. Polarized Light. 2nd ed. New York: Marcel Dekker Inc.; 2003. 680 p. ISBN: 082474053-X

[42] Ultra Precision Low Profile ™ Load Cell Interface Force™. [Internet] Available: http://www.interfaceforce.com/index.php?mod=product&show=3 [Accessed: 2020-06-01].

[43] Detroit Calibration Lab Trescal. [Internet] Available: http://www.trescal.us/calibration-lab/michigan/detroit/detroit-calibration-lab [Accessed: 2020-06-01].

[44] Bartel T, Yaniv S, Seifarth R. Force measurement services at NIST: Equipment, procedures, and uncertainty. In: NCSL Workshop & Symposium. 1997. pp. 421-431

[45] Method for Lifting Device Motion Parameters Controlling, by Poyarkov A, Barakov V, Paulish A, Shatov V, Fedorinin V. Patent RU 2618862. 2015, October 15. [Internet] Available: https://www1.fips.ru/ofpstorage/Doc/IZPM/RUNWC1/000/000/002/618/862/%D0%98%D0%97-02618862-00001/document.pdf [Accessed: 2020-06-01].